MCDONNELL DOUGLAS ASTRONAUTICS COMPANY • EAST

MCDONNELL DOUGLAS CORPORATION

CONTENTS

EFFECTIVE PAGES

Title

ii through iv

1 through 32

ABSTRACT

An experimental investigation was conducted on Space Shuttle type, body-wing configurations in the Martin-Marietta Corporation, Denver Division, Hotshot facility. The purpose of the investigation was to determine the effects of body and wing geometry on the hypersonic shock structure about these vehicles and on the resulting surface impingement of interior flow field shock and expansion waves. Schlieren photographs and thermographic phosphor paint data were obtained on three body cross sections with three wing planforms at 40, 50 and 60 degree angles of attack. Specific configuration data were obtained at 0 and 30 degree angles of attack to develop trends. These data were obtained at a nominal Mach number of 13.5 and a freestream unit Reynolds number of 0.7×10^6 per foot.

For comparison with these "straight wing" configurations, data were also obtained on a model of a point design, high cross-range, delta wing orbiter at 40, 50 and 60 degree angles of attack. As expected, the data on this delta wing orbiter indicated that the shock intersection/impingement phenomena associated with straight wing vehicles are considerably more complex than, and result in both windward and leeward surface heating regions not present on, the delta configuration.

Although the delta configuration tests are shown in the schedule, the results are not discussed in this report, since no regions of shock wave interaction or impingement comparable with the winged configuration were found in the results.

This study was conducted under contract NAS-9-11082.

NOMENCLATURE

c	Wing root chord
H	Altitude
M_∞	Freestream Mach number
r_c	Body corner radius
Re_∞/Ft	Freestream unit Renolds number
S	Wing span
V_∞	Freestream velocity
W_b	Fuselage width
W/SC_L	Glide parameter
Y_I	Intersection point, measured from centerline
α	Angle of attack
γ	Specific heat ratio

1. INTRODUCTION

The Space Shuttle program has focused interest on many technological problems for which even the most sophisticated analytical tools are inadequate. Among these problems, the deficiency in flow field methodology can be traced directly to inability to compute realistic three-dimensional flow fields over the complex Space Shuttle configurations for the range of flight variables required. To overcome this obstacle, experimental investigations on Space Shuttle type configurations are being conducted to obtain data which provide an understanding of the critical problems associated with the Space Shuttle program.

Figures 1 through 4 illustrate typical flight trajectory parameters for a Space Shuttle mission (Booster/Orbiter ascent, Booster fly-back and high and low cross-range Orbiter fly-back). Mach number and angle of attack histories required by the mission generate a host of complex specialized problems. This report addresses one such problem: the effect of wing-body configuration on wing shock impingement phenomena. The results and analysis presented here were obtained under contract NAS-9-11082 for the experimental study of "Shock Wave Impingement Phenomena on Space Shuttle Vehicles."

Initially, this program was to provide parametric data on various straight wing configurations. Under these groundrules, a hypersonic test program was defined which would indicate the effect of body shape, wing geometry, and angle of attack on body-wing shock intersection and impingement parameters. Midway through the program, a delta wing configuration was added to the test matrix, to reflect NASA's decision to drop the low cross-range Orbiter configuration in favor of the high cross-range, delta wing, Orbiter. The test matrix was expanded by incorporating selective test shots using the McDonnell Douglas delta wing Orbiter. Prime emphasis, however, remained on the original task; a parametric study of the effect of various wing-body combinations on shock impingement phenomena at high angles of attack (40 to 60 degrees). Although the test conditions of this program are more representative of Orbiter flight conditions (Mach number), the results are equally applicable to winged Booster configurations. Likewise, although the winged configurations are discussed with respect to the low cross-range Orbiter, the results are applicable to swept winged Orbiter with sufficient hypersonic lift-drag ratio capability to meet the high cross-range requirements.

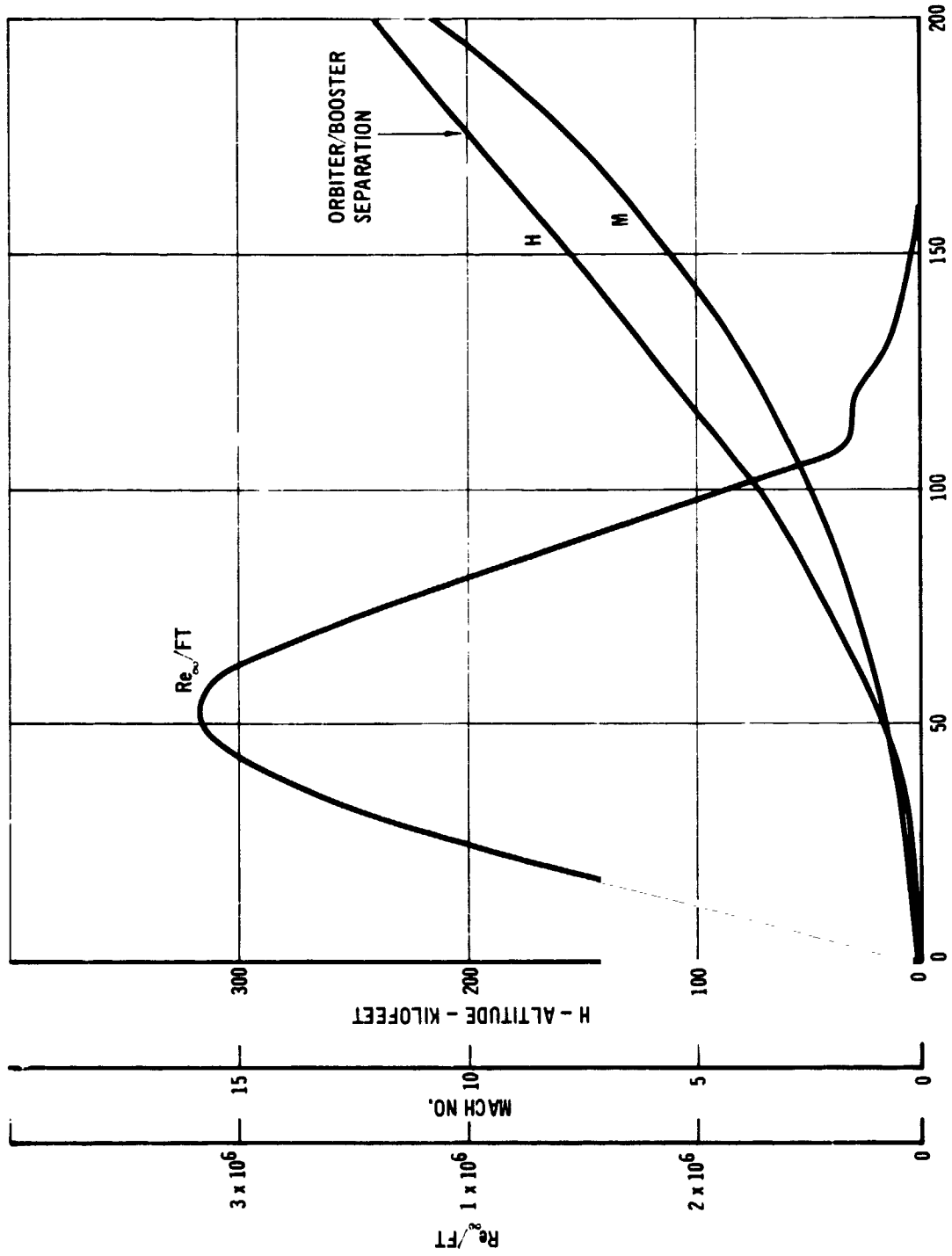

FIGURE 1 ASCENT TRAJECTORY OF BOOSTER/ORBITER

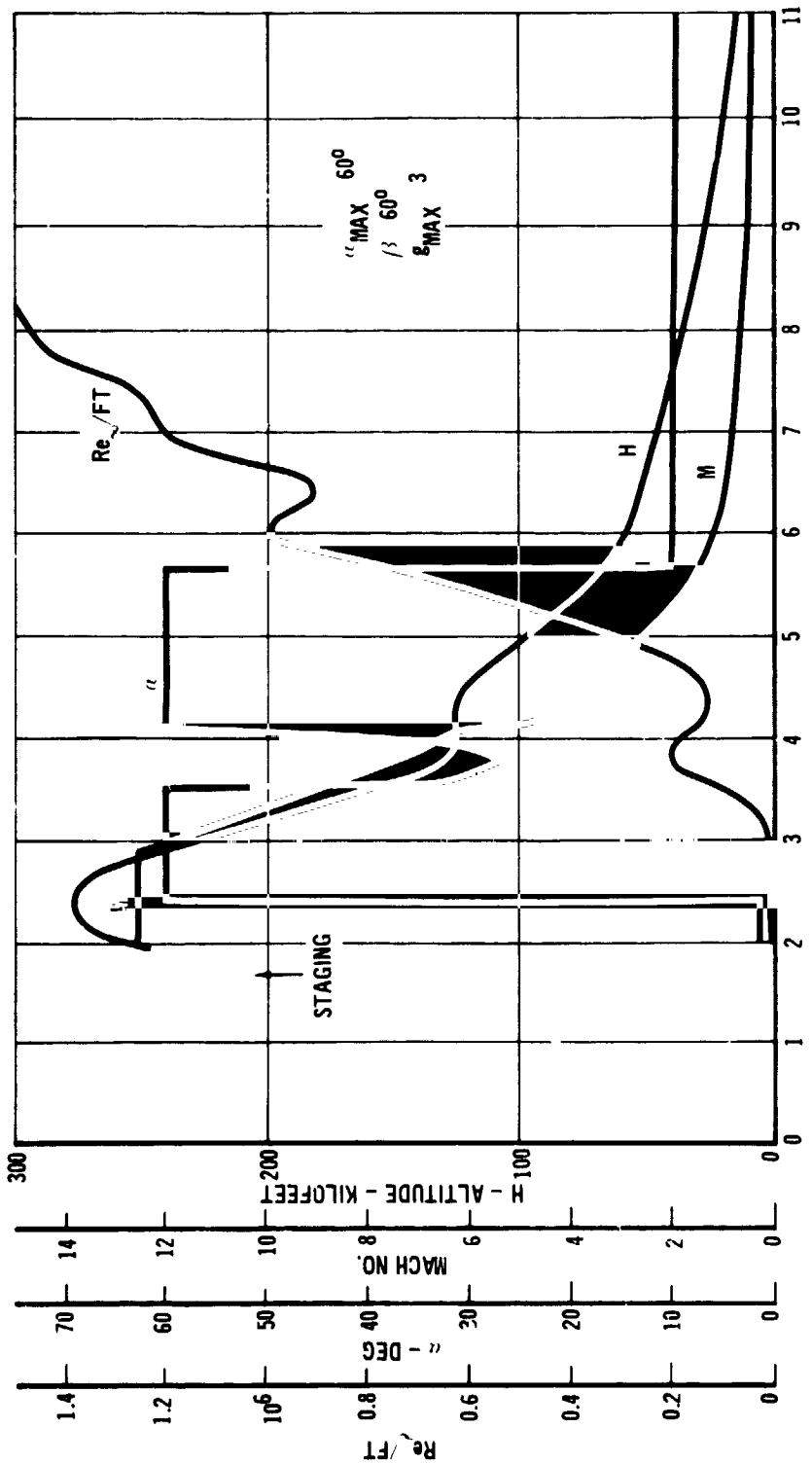

FIGURE 2 NOMINAL BOOSTER REENTRY TRAJECTORY

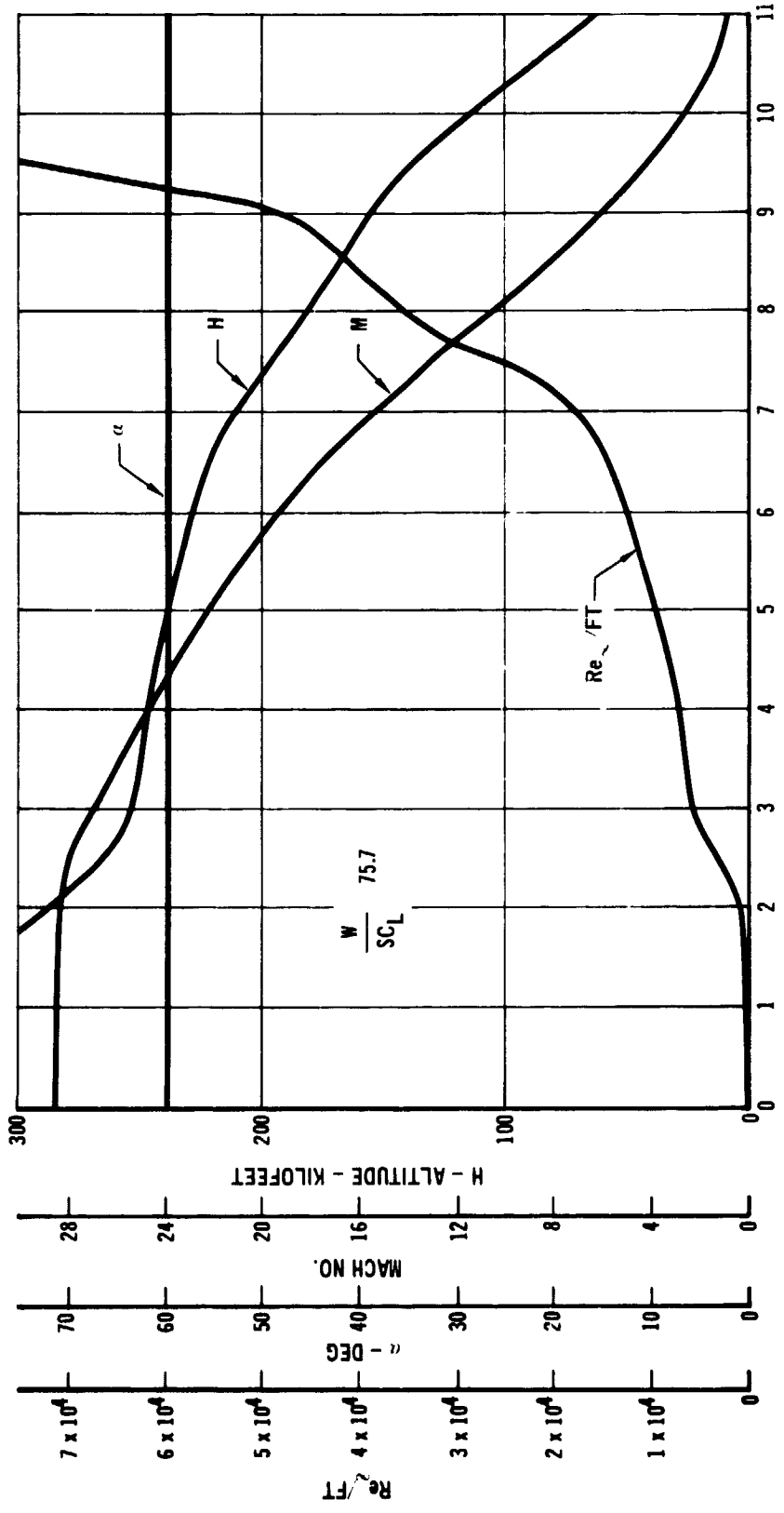

FIGURE 3 LOW CROSS-RANGE ORBITER ENTRY TRAJECTORY

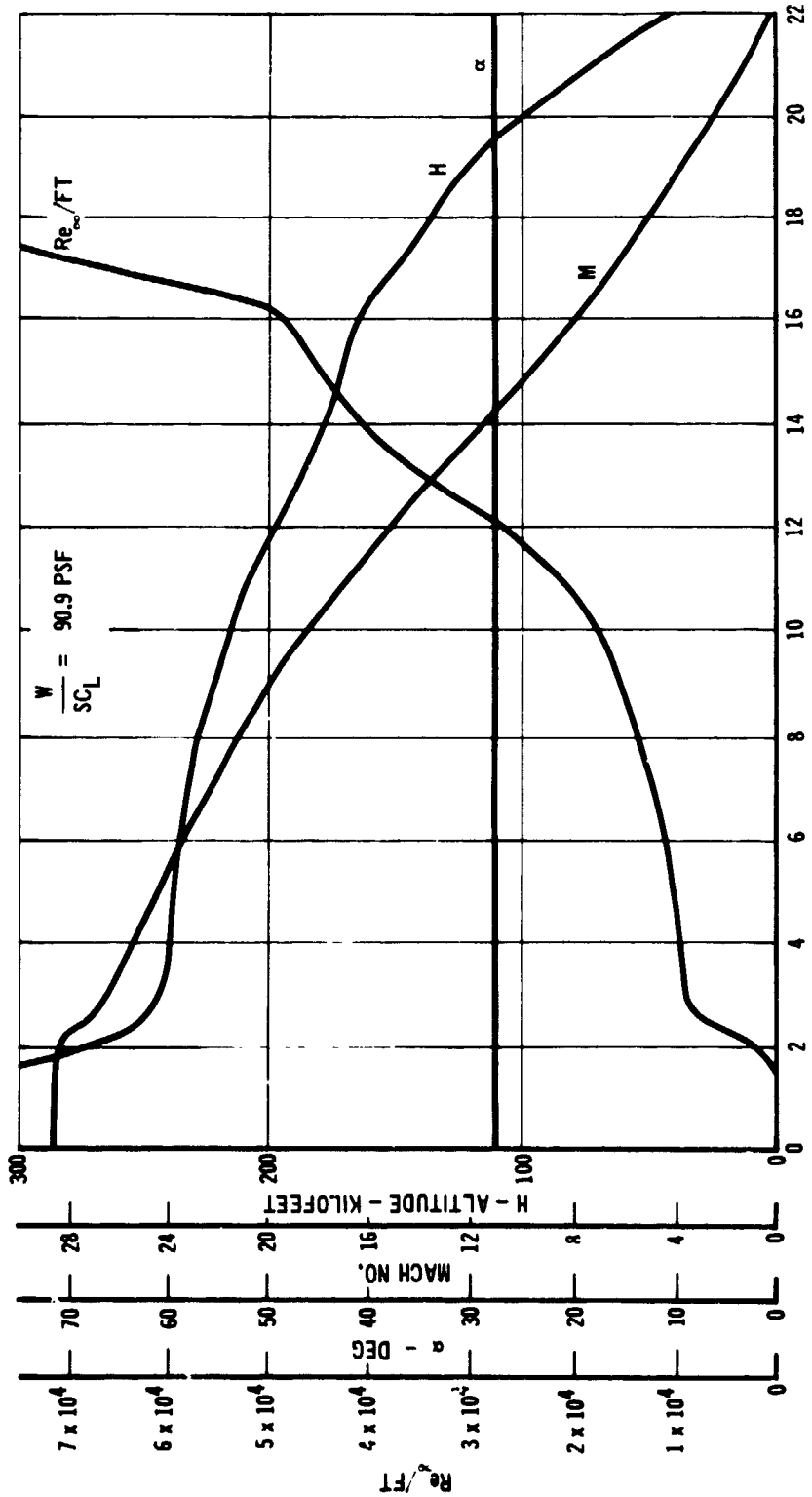

FIGURE 4 HIGH CROSS-RANGE ORBITER ENTRY TRAJECTORY

2. MODELS AND TEST SCHEDULE

MODELS

Model design was focused on representative body cross sections and wing planforms. The basic configurations tested were similar; the straight wings were located in the same position and the cylindrical fuselages were faired to a given nose cap shape. These general features are shown in figure 5.

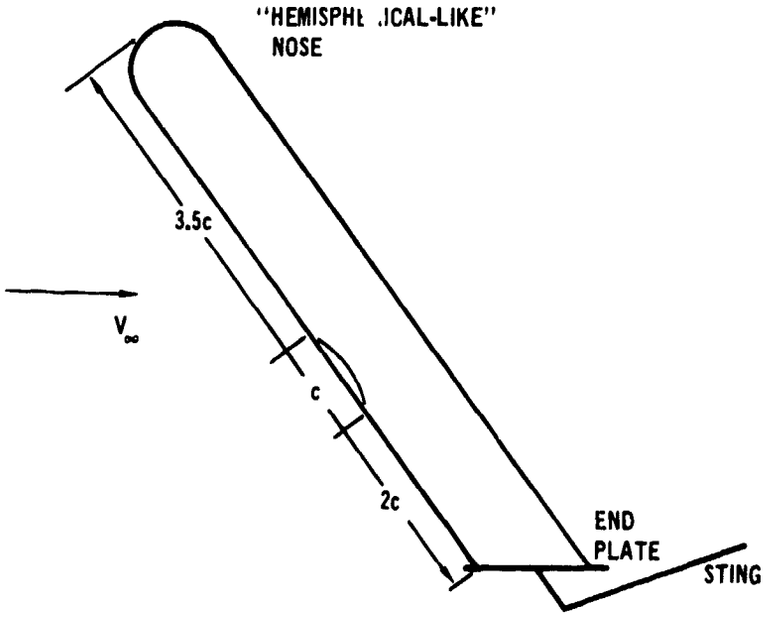

FIGURE 5 GENERAL FEATURES OF TEST CONFIGURATIONS

Figure 6 defines the three basic body cross sections (C1, C2, and C3) tested during the program; alterations in configurational cross section were incorporated by changing the corner radius, r_c. The "key" for defining the cross section's ratio of corner radius to body width is indicated in figure 6. The notation "C2, a" refers to a cylindrical configuration with a cross section given by configuration 2 (C2) of figure 6, with a ratio of corner radius to body width of 0.02.

Three different wing planforms were tested with each of the cylindrical bodies. The wings (defined by figure 7) are identified as W1, W2, and W3. All three wings have a NACA 0012-64 airfoil cross section.

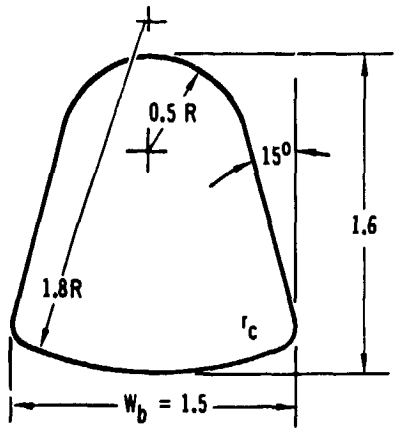

CONFIGURATION 1: C1

MODIFICATIONS:

KEY	r_c/W_b
0	0
a	0.02
1	0.0625
2	0.125

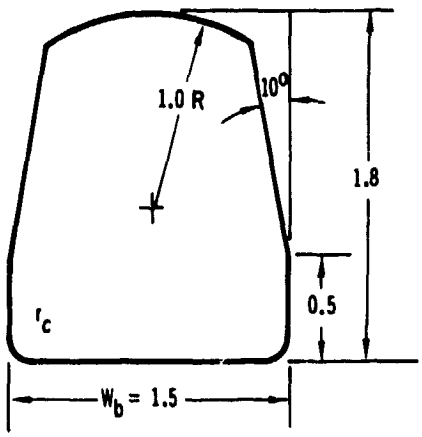

CONFIGURATION 2: C2

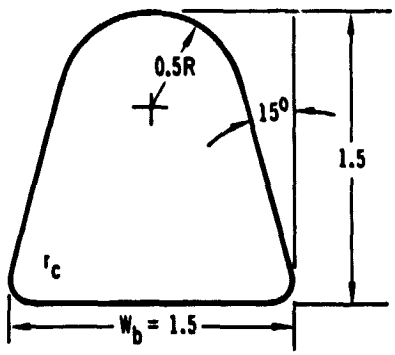

CONFIGURATION 3: C3

FIGURE 6 CYLINDRICAL CROSS-SECTIONS TESTED

W2 IS THE MOST TESTED WING CONFIGURATION AND HAS THE FOLLOWING FEATURES:

- NACA 0012–64 AIRFOIL
- 15 DEG LEADING EDGE SWEEP
- S = 2 TIMES MOLD-LINE CHORD
- MOLD-LINE CHORD = 0.75 W_b

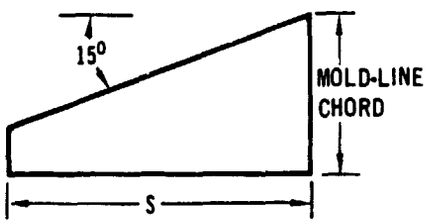

W1 IS SIMILAR TO W2 EXCEPT THE LEADING EDGE SWEEP IS 0 DEG

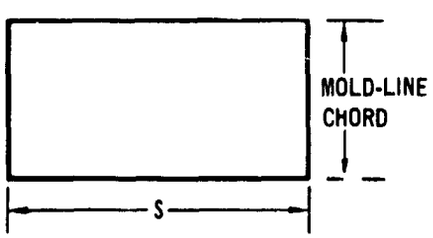

W3 IS SIMILAR TO W2 EXCEPT THE LEADING EDGE IS SWEPT 30 DEG
AND TRAILING EDGE IS SWEPT 17.5 DEG

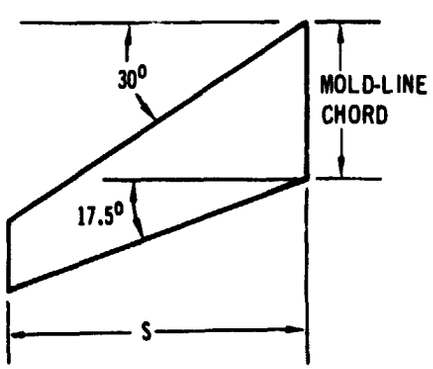

FIGURE 7 WINGS TESTED

A test configuration is, therefore, uniquely defined when its cross section, corner radius, and wing (planform) are specified. The following notation will be used throughout this report to indicate particular test configurations:

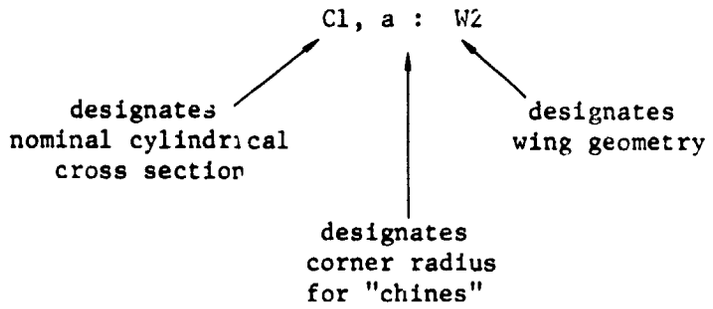

TEST SCHEDULE

The Phase 1 test program was conducted in the Martin-Marietta Hotshot facility using white epoxy painted wood models, which were coated with thermographic phosphor paint for thermal mapping. Table 1 summarizes the original portion of this straight wing test program. Table 2a illustrates, in compact form, which wings were tested with which bodies.

Table 2b describes the supplementary straight wing test program and the delta wing test program conducted after the completion of the initial test plan.

TABLE 1 TEST MATRIX

CONFIGURATION*	α	M_∞	Re_∞/FT	HEAT TRANSFER	SCHLIEREN (VIEW FROM:)
C1, 0:W2	50^0	13.5	0.7×10^6	YES (1)	WINDWARD
C1, 0:W2	60^0	↓	↓	YES (2)	LEEWARD
C1, 2:W1	44^0	↓	↓	YES (2)	LEEWARD
C1, 1:W1	40^0	↓	↓	YES (1)	WINDWARD
C1, 1:W1	50^0	↓	↓	YES (2)	LEEWARD
C1, 1:W1	60^0	↓	↓	YES (2)	LEEWARD
C1, 1:W2	40^0	↓	↓	YES (1)	WINDWARD
C1, 1:W2	50^0	↓	↓	YES (1)	WINDWARD
C1, 1:W2	60^0	↓	↓	YES (2)	LEEWARD
C1, 1:W3	40^0	↓	↓	YES (1)	WINDWARD
C1, 1:W3	50^0	↓	↓	YES (2)	LEEWARD
C1, 1:W3	60^0	↓	↓	YES (2)	LEEWARD
C1, 2:W2	40^0	↓	↓	YES (2)	WINDWARD
C1, 2:W2	50^0	↓	↓	YES (2)	LEEWARD
C1, 2:W2	60^0	↓	↓	YES (2)	LEEWARD
C1, a:W2	40^0	↓	↓	YES (1)	WINDWARD
C1, a:W2	50^0	↓	↓	YES (2)	LEEWARD
C1, a:W2	60^0	↓	↓	YES (2)	LEEWARD
C2, 0:W2	40^0	↓	↓	YES (1)	WINDWARD
C2, 0:W2	50^0	↓	↓	YES (1)	WINDWARD
C2, 0:W2	60^0	↓	↓	YES (1)	WINDWARD
C2, 1:W2	40^0	↓	↓	YES (1)	WINDWARD
C2, 1:W2	50^0	↓	↓	YES (2)	LEEWARD
C2, 1:W2	60^0	↓	↓	YES (2)	LEEWARD
C3, 1:W2	40^0	↓	↓	YES (1)	WINDWARD
C3, 1:W2	50^0	↓	↓	YES (1)	WINDWARD
C3, 1:W2	60^0	13.5	0.7×10^6	YES (2)	LEEWARD

* CONFIGURATION NOTATION DEFINED BY FIGURES 6 AND 7
(1) WINDWARD SURFACE OF WING
(2) LEEWARD SURFACE OF WING
(3) SIDE SURFACE OF BODY

TABLE 2 SUMMARY AND SUPPLEMENTAL TESTS

TABLE 2A SUMMARY OF ORIGINAL TEST PLAN

BODY \ WING	W1	W2	W3
C1,0		X	
C1,1	X	X	X
C1,2		X	
C1,a		X	
C2,0		X	
C2,1		X	
C3,1		X	

TABLE 2B: SUPPLEMENTAL TESTS

CONFIGURATION*	α	M_∞	Re_∞ /FT	HEAT TRANSFER	SCHLIEREN (VIEW FROM:)
C1,1:W3	40^0	13.5	0.7×10^6	YES (3)	SIDE
C1,1:W3	50^0	13.5	0.7×10^6	YES (3)	SIDE
C1,1:W3	60^0	13.5	0.7×10^6	YES (3)	SIDE
C1,2:W2	30^0	13.5	0.7×10^6	NO	WINDWARD
C1,2:W2	0^0	13.5	0.7×10^6	NO	WINDWARD
MDC DELTA	60^0	13.5	0.7×10^6	NO	SIDE
	60^0				WINDWARD
	50^0				SIDE
	50^0				WINDWARD
	40^0				SIDE
MDC DELTA	40^0	13.5	0.7×10^6	NO	WINDWARD

* CONFIGURATION NOTATION DEFINED BY FIGURES 6 AND 7
(1) WINDWARD SURFACE OF WING
(2) LEEWARD SURFACE OF WING
(3) SIDE SURFACE OF BODY

3. HOTSHOT TEST FACILITY

The Martin Marietta Hypervelocity Impulse Wind Tunnel[1] (Hotshot) is an intermittent hypersonic aerodynamic test facility. The stagnation temperatures and pressures necessary to produce a hypersonic flow are provided by striking a high energy arc (driven by a large capacitor bank) in a pressure chamber which has previously been filled with dry nitrogen. Pressure in the chamber increases sharply and bursts the aluminum diaphragm, allowing the nitrogen to flow through the evacuated hypersonic nozzle to the test section, diffuser, and dump tank.

Maximum available capacitor storage is 800,000 joules at 12,000 volts. Lower energies are obtained by lowering the charge voltage. Arc discharge chambers of 150 and 210 cubic inch capacity are used; the desired size is determined by the required test Mach number. The test Mach number is a function of the variable nozzle throat size setting. Pressures and temperatures attainable in the arc chamber range from 5,000 to 20,000 pounds per square inch, and from 1500 to 3500°K, respectively. These conditions drive the nozzle to Mach numbers from 13 to 24, and a Reynolds numbers range from 0.12×10^6 to 1.2×10^6 per foot. Flow duration is 50 to 100 milliseconds, with a 10 to 30 millisecond starting period.

The aluminum diaphragm is sheared cleanly by a steel punch and then caught by a baffle in a settling chamber which separates the arc chamber and nozzle. This prevents diaphragm debris from entering the nozzle, and results in a low level of flow contamination in the test section. The baffle and settling chamber combination also removes particles evaporated in the arc chamber from the flow.

All data obtained are recorded on a fourteen track analog tape deck. Six channels are required for flow condition measurements (arc chamber pressure, test section pitot pressure, and test section stagnation heating). The remaining eight channels are available for force and moment, or temperature or pressure measurements from the model. Additional tape decks are available if more channels are required. The analog tape is digitized with data points every 0.8 milliseconds during the run and the data reduced, using the enthalpy technique[2], to test conditions and model measurements.

4. DATA REDUCTION

Double-pass color schlieren system photographs were taken during each shot. The schlieren photographs were taken from the windward, leeward, or side view by rotating the model in the tunnel. Tables 1 and 2 document the view for each of the runs. Figure 8 is typical of the data obtained. Note that the wing-body shock intersection is clearly indicated through a sudden change in the flow structure over the wing. The distance of this intersection point from the body centerline (denoted by Y_I) was measured from each schlieren photograph three separate times to eliminate errors and to ensure consistency. For only a few shots did the repeat measurements differ by more than 5 percent from the original measurement.

High contrast burn photographs were taken following each shot to determine the shock impingement location on the wing windward surface. This burn pattern developed on the model surface when the windward heating rate scorched the white epoxy paint covering the wooden model. Following each run, the models were cleaned and repainted. Figure 9 is representative of the burn photographs. For most of the shots, the burn data clearly indicated discrete hot spots on the leading edge. Some of the photographs show the burn angle on the wing windward surface, but these data were not available for enough runs to provide an analysis of the impingement angle. The distance of the leading edge burn location from the body centerline was also measured three separate times.

A thermographic mapping technique was used to determine aerodynamic heating patterns on the model surfaces. A thin, lacquer based coating of a temperature sensitive phosphor was sprayed on the test model prior to each run. The model was then illuminated with ultra-violet light during the test. A photograph of the model was taken prior to, and during, the test run (the configuration surface viewed for each run is indicated in tables 1 and 2). Since the phosphor coating emits light in inverse proportion to the surface temperature (reaction time is on the order of 1 millisecond), the intensity patterns in the resulting photograph may be traced to indicate contours of constant density and, hence, surface temperature on the model.

Spanwise temperature distributions for selected runs were calculated based on the thermographic mapping data. Phosphor number 1807 was used for all leeward side mappings, since it is in a linear range over the temperature range encountered (near room temperature) (refer to figure 10). The level of ultraviolet excitation

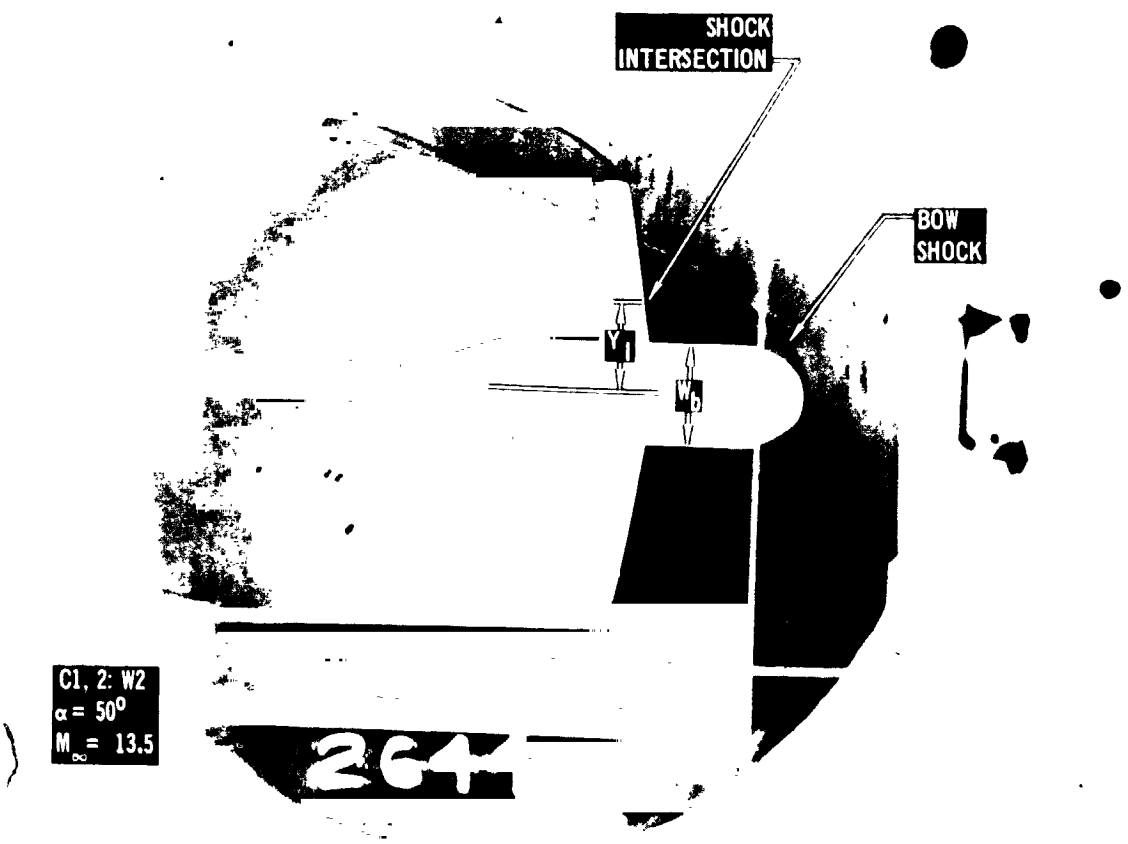

FIGURE 8 TYPICAL SCHLIEREN

D4C 86310

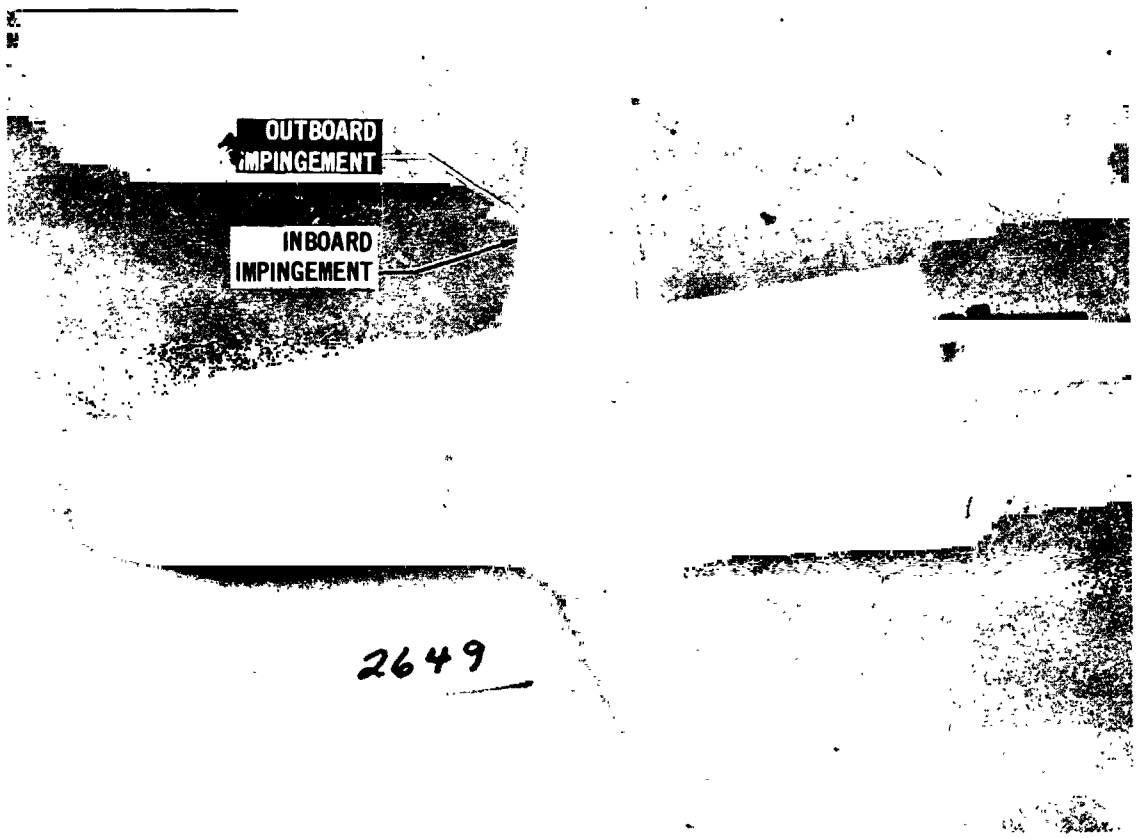

FIGURE 9 BURN PHOTOGRAPH

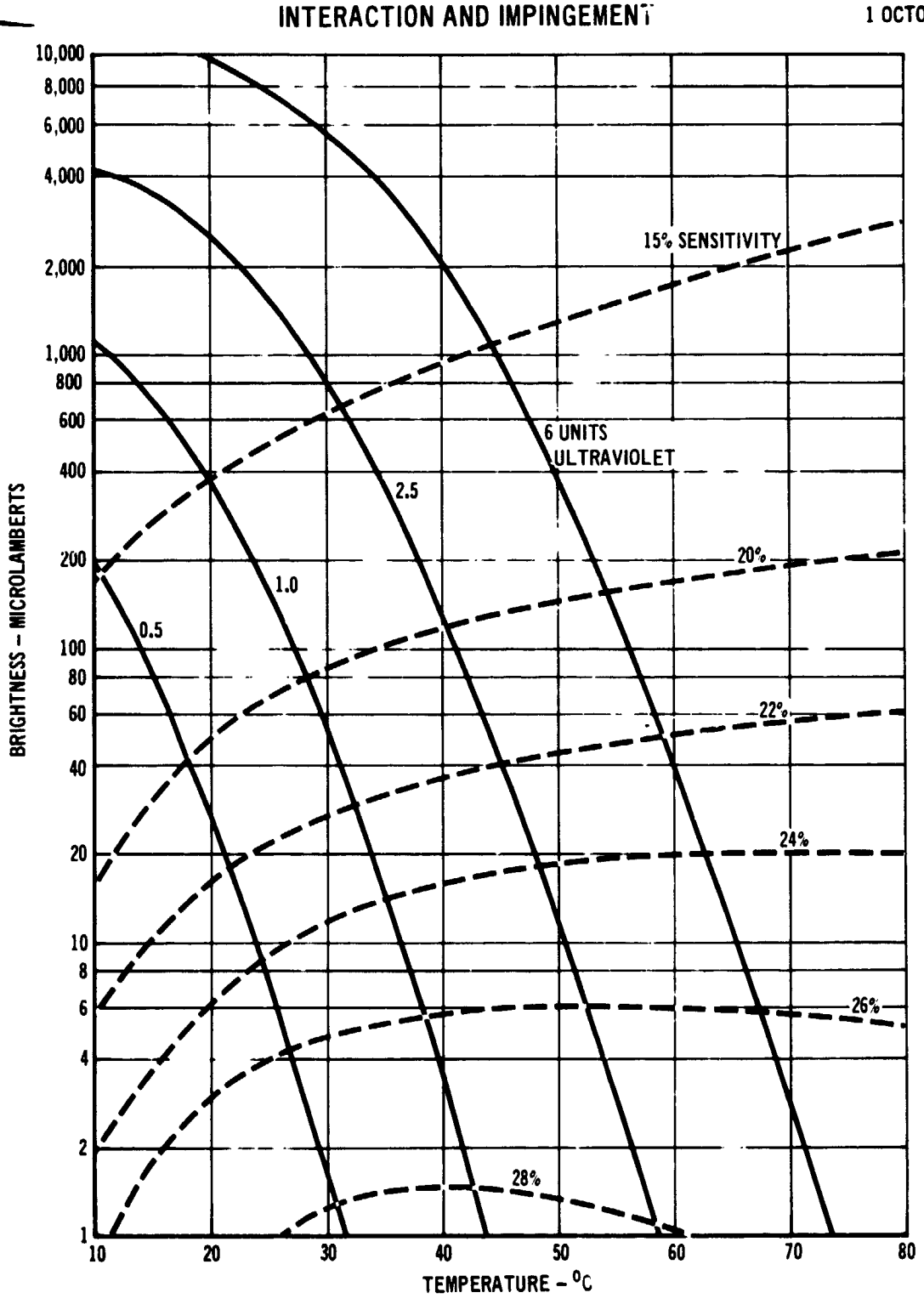

FIGURE 10 PERFORMANCE OF RADELIN THERMOGRAPHIC PHOSPHOR NO. 1807

SOLID CURVES SHOW BRIGHTNESS AGAINST TEMPERATURE AT FOUR LEVELS OF ULTRAVIOLET EXCITATION. DASHED CURVES SHOW SENSITIVITY (PERCENT BRIGHTNESS CHANGE PER DEGREE CENTIGRADE CHANGE OF TEMPERATURE) AGAINST BRIGHTNESS AND TEMPERATURE

is 1.0. Therefore, variations in phosphor brightness between the no-flow and flow cases can be related directly to temperature changes above or below room temperature.

In reducing the thermographic data, the film density of the photographs is assumed to be directly proportional to phosphor brightness. A spanwise scan, at midchord, is made of both the no-flow and the flow photographs with a MacBeth diffuse densitometer. These film density data are plotted against spanwise position which, in turn, permits calculation of a change in phosphor brightness for any wing station (refer to figure 11). The temperature/brightness relation for phosphor 1807 is then used to convert the brightness change to a temperature change above or below 22°C.

A primary limitation of this technique is the background film density, since film density changes below the background level can not be resolved. Therefore, very high temperature areas on the wing can only be said to be equal to, or greater than, the resolution limited temperature.

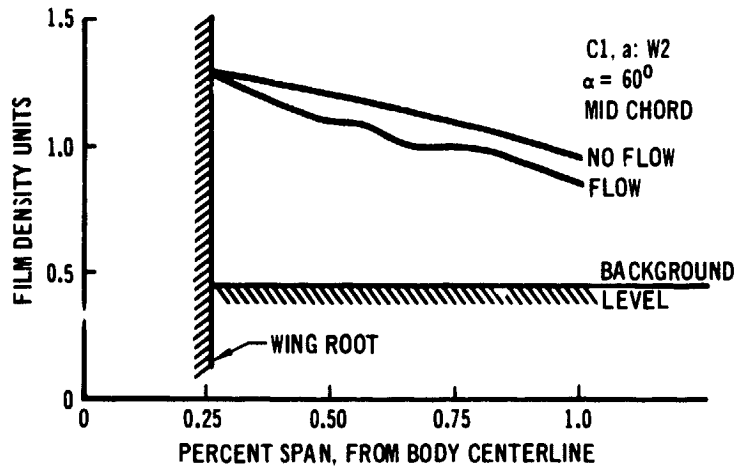

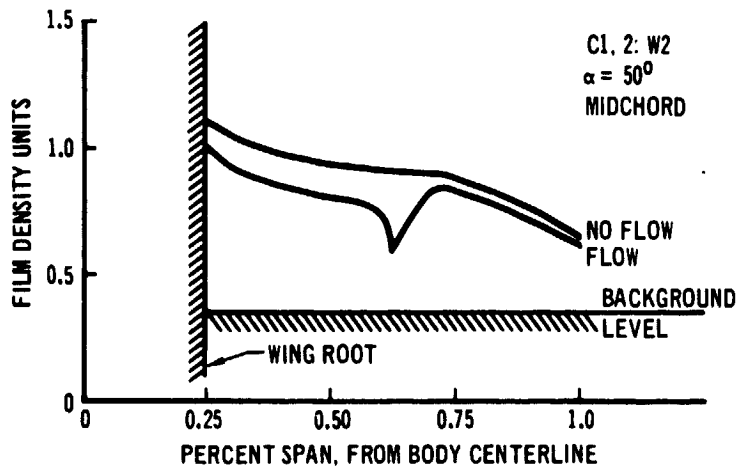

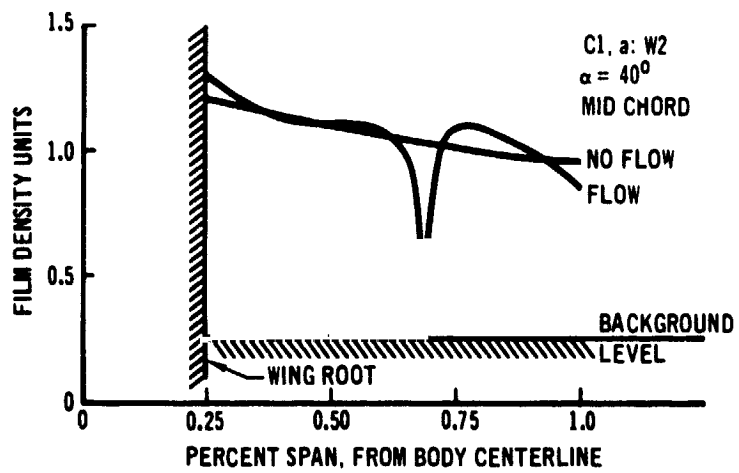

FIGURE 11 FILM DENSITY AS A FUNCTION OF SPAN LOCATION

5. RESULTS AND DISCUSSION

The wing-body shock wave intersection, and the resulting wing surface impingement, are both complex three-dimensional flow field phenomena which are configuration dependent. The relative strengths of the body and wing shock determine the class of shock interaction[3], impingement structure, and the associated severity of surface heat transfer.

Shock Intersection - The colored schlieren photographs were analyzed to determine the shock intersection location as a function of configuration and angle of attack. Data obtained from the "most tested" wing planform, W2, provide the best basis for detailed review.

As a basis for limit comparison with the high angle of attack test results, two theoretical predictions were made to predict the body-wing shock intersection point at zero degrees angle of attack. For the computations, the body was assumed to be axisymmetric, with the planform as the equivalent cross section. The results of the two predictions, along with experimental results obtained at the end of the test program, are presented in figure 12. The "correlation" shock shape was pre-

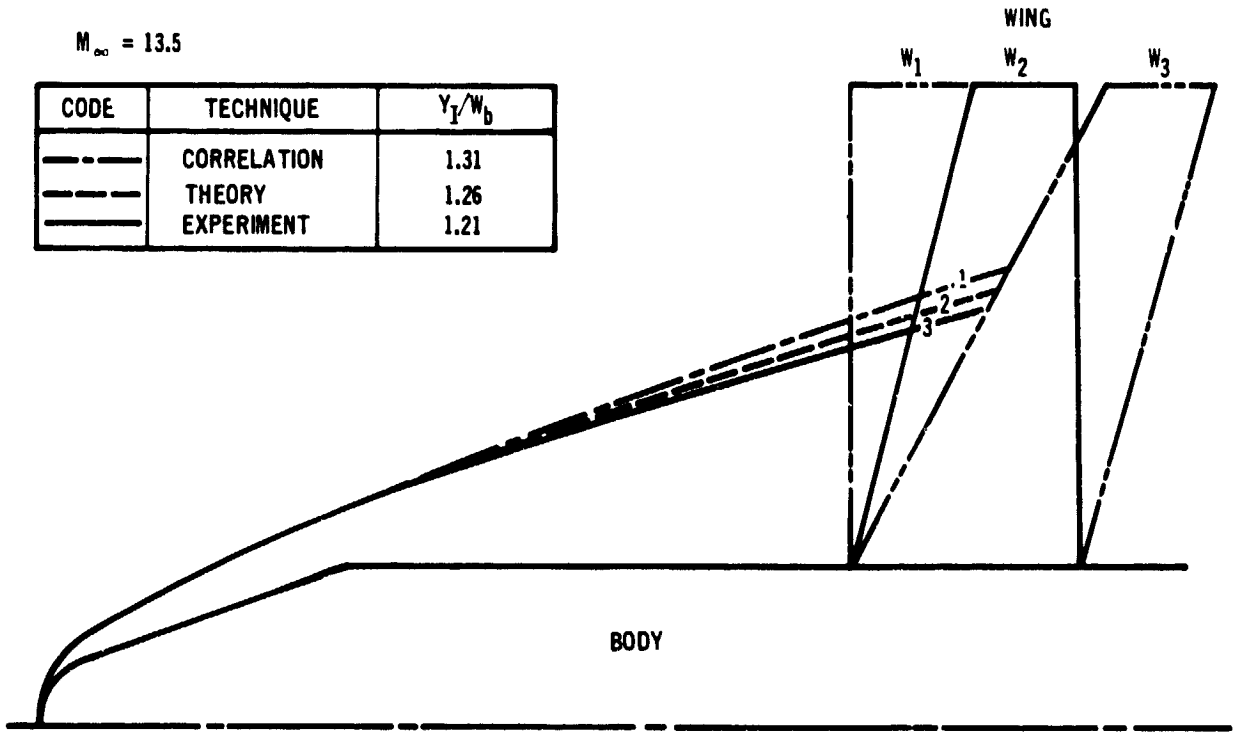

FIGURE 12 ZERO ANGLE OF ATTACK SHOCK SHAPE

dicted from hemisphere-cone[4] correlations and a Prandtl-Meyer expansion. The "theory" shock shape was computed with inverse-blunt-body and rotational method of characteristics computer program calculations. As the test program progressed, it became evident that low angle of attack data would be invaluable for trend prediction. Therefore, configuration C1,2:W2 was also tested at 0 and 30 degree angles of attack. The results show that both theoretical predictions are in good agreement with the zero angle of attack experimental data. For the other configurations, the theoretical predictions are used to define the 0 degree angle of attack shock intersection location.

The effect of increasing the vehicle angle of attack on the body-wing shock intersection location is shown in figure 13. Data are available for 0, 40, 50,

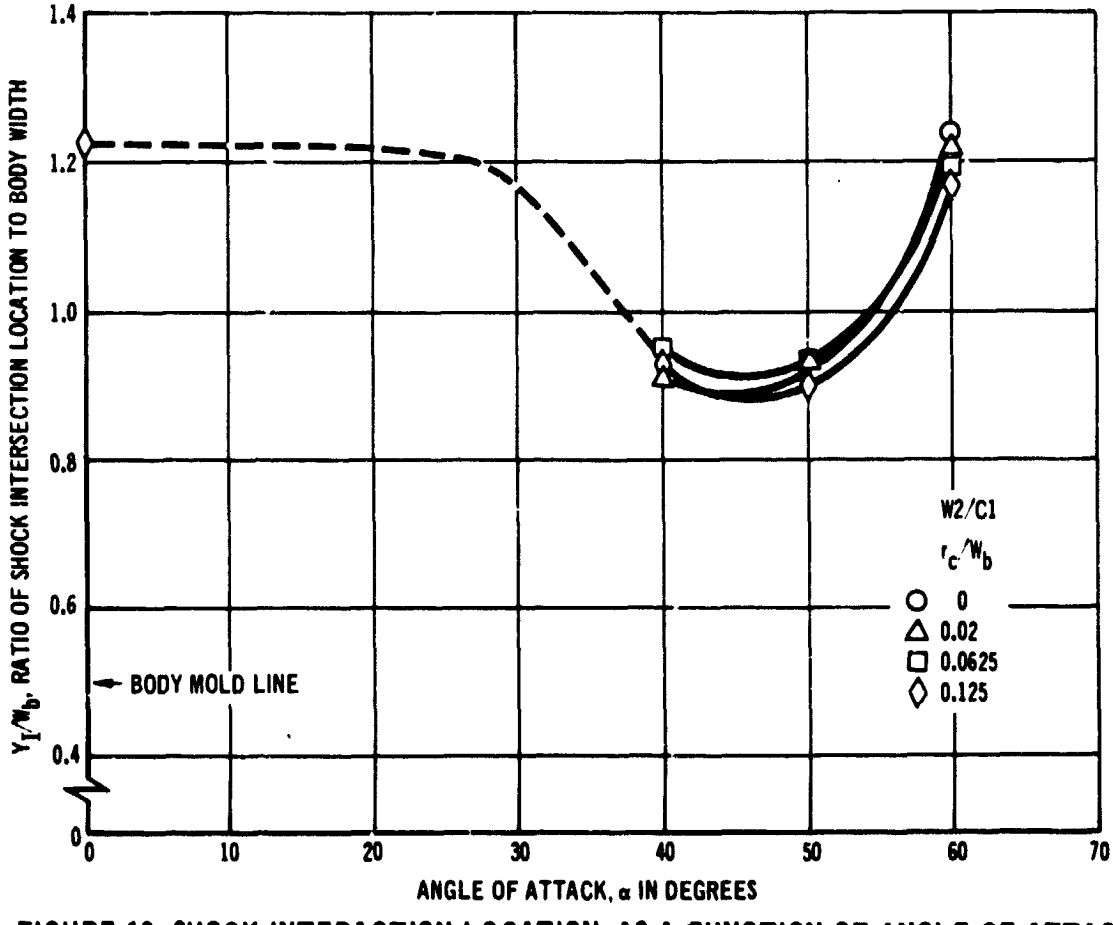

FIGURE 13 SHOCK INTERACTION LOCATION AS A FUNCTION OF ANGLE OF ATTACK

and 60 degree angles of attack. As the angle of attack is increased from 0 toward 40 degrees, the shock envelope appears to be almost unaltered as the body nestles down into the windward surface of the shock. The effect is to move the shock interaction inboard toward the body mold line as the angle of attack increases from about 30 degrees upwards.

Furthermore, as angle of attack increases, the pressure ratio across the body shock also increases. When the pressure ratio across the body shock increases to the point at which it "detaches," the inboard movement of the shock intersection "buckets" and the new shock structure is postulated as follows: the body and wing shocks become coplaner and merge into a single shock envelope (the configuration planform becoming some "cruciform-shaped" equivalent blunt body) thereby causing the observed shock intersection point to move rapidly outboard and disappear. Figures 14 and 15 indicate the same trends for test configurations C2:W2 and C3:W2.

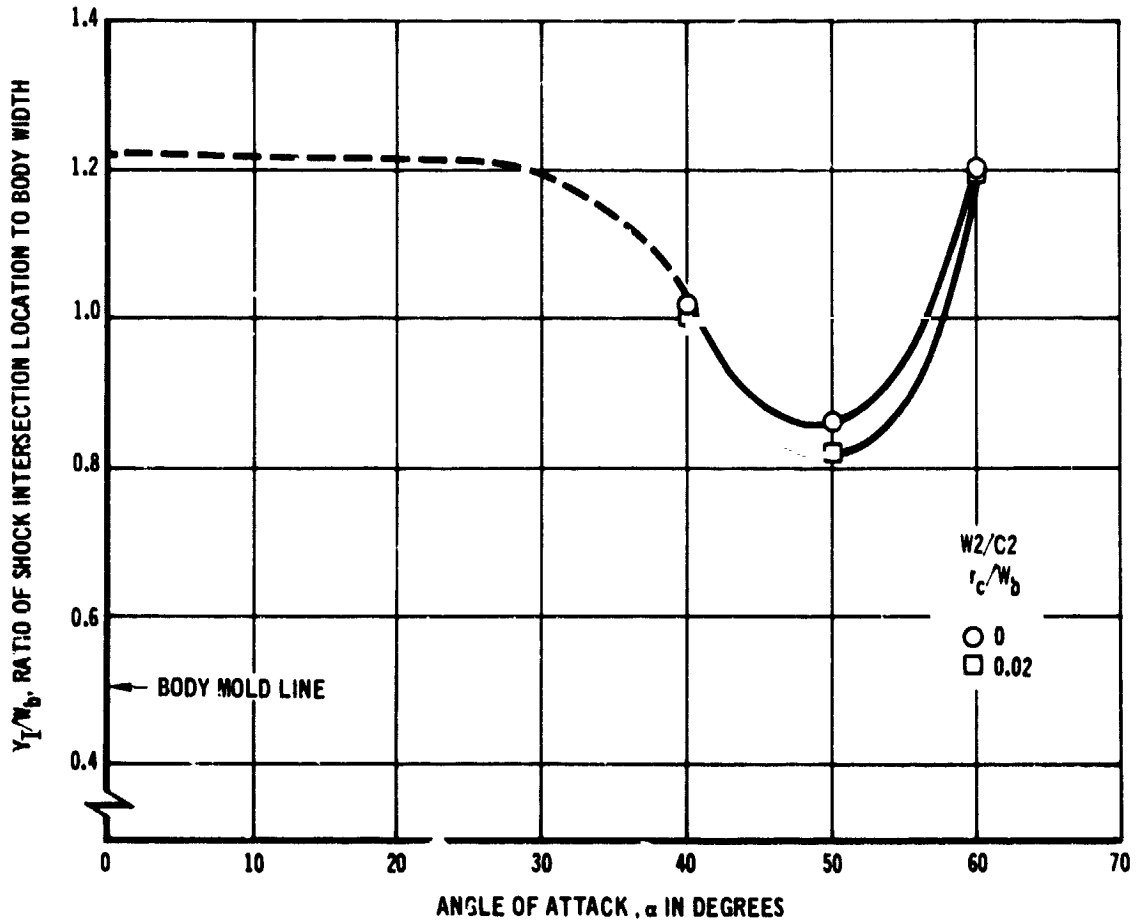

FIGURE 14 SHOCK INTERSECTION LOCATION AS A FUNCTION OF ANGLE OF ATTACK

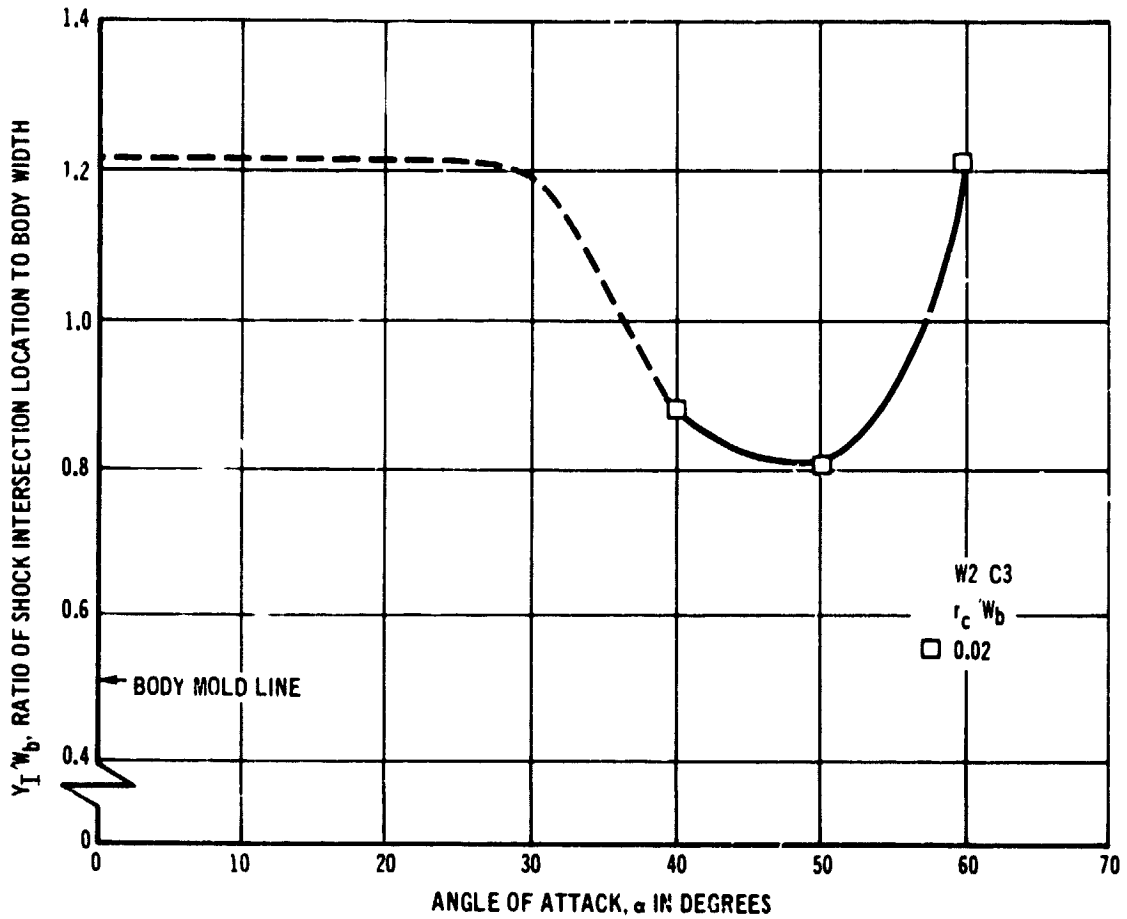

FIGURE 15 SHOCK INTERSECTION LOCATION AS A FUNCTION OF ANGLE OF ATTACK

The "bucket" observed is based on the limited 60 degree angle of attack data. Therefore, the possibility exists that the intersection point may move outboard rapidly, or it may simply disappear when the shocks become coplaner, yielding a discontinuous trend as a function of angle of attack.

As the corner radius of the body cross section is increased, the body shock wave is altered downstream of the corner. Inviscid flow theory indicates that rounding the corner (toward the limiting configuration of a cylinder) draws the bow-shock in the direction of the afterbody. This effect has also been verified experimentally for body along shuttle-like configuration in cross-flow[5]. The movement of the bow-shock toward the body would indicate that the body-wing shock intersection location should move inboard on the wing with increasing corner radii. Figure 16 indicates the effect of rounding the corner on the body-wing shock intersection location for configuration C1. For a specified angle of attack (40, 50, and 60 degrees), the intersection point is observed to move slightly inboard with

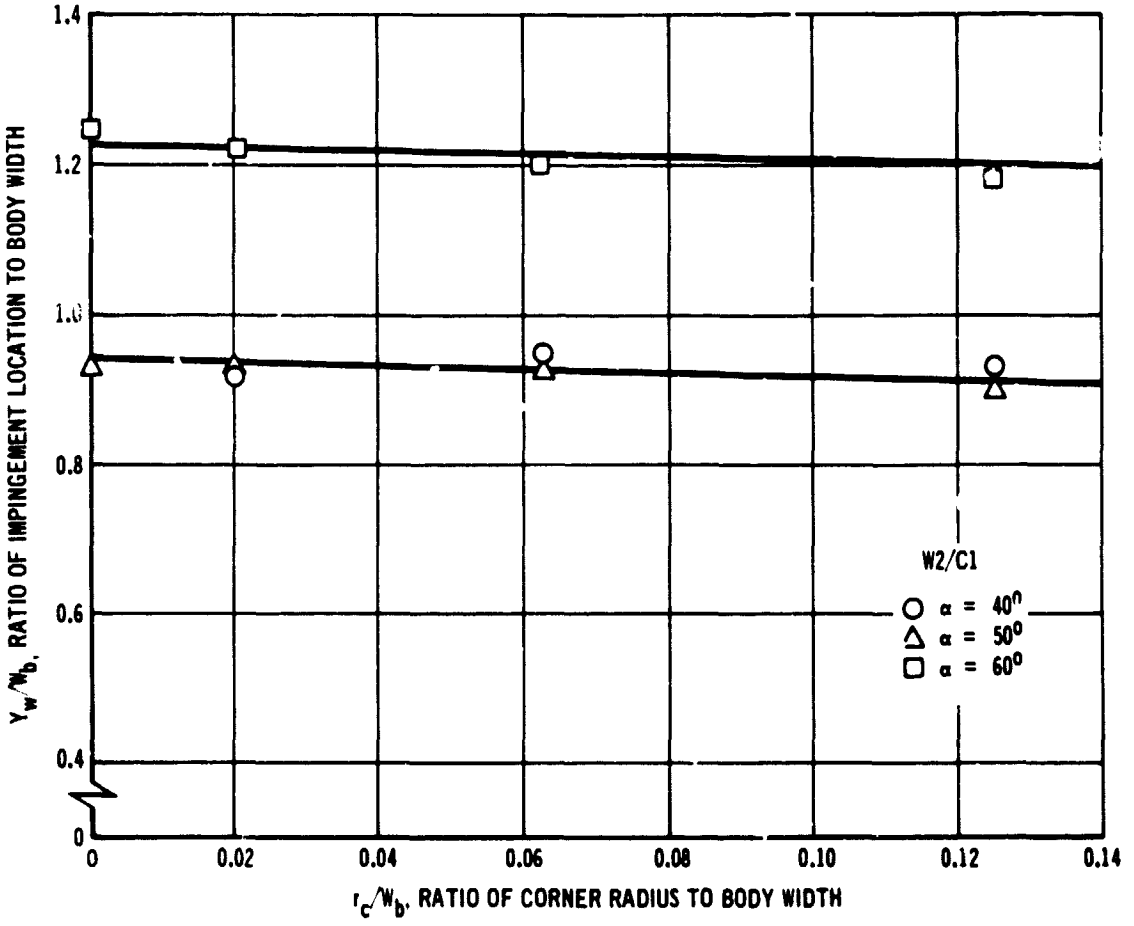

FIGURE 16 SHOCK INTERACTION LOCATION AS A FUNCTION OF CORNER RADIUS

increasing corner radius. Figure 17 indicates the same effort of body corner radius for configuration C2:W2. Supporting data (burn photographs and thermographic phosphor patterns) indicate that, for the range of corner radii tested, the rather weak dependence of intersection location on corner radius is not sufficient to change the resulting wing impingement phenomena. This does not imply that the type of interaction cannot change; rather, it shows that, for these models and test conditions, a change was not observed.

Wing Impingement - Burn pattern data (all on windward surfaces) are presented only for test configuration C1:W2 since, as with the shock interference data, this was the most tested configuration. The burn pattern clearly indicates a stagnation line near the wing leading edge on the windward surface. Two regions of high heating are consistently present for the 40 and 50 degree angles-of-attack data. These high heating regions emanate from the leading edge and form an "M" shaped pattern with vertices at the leading edge. The 60 degree angle-of-attack data do not exhibit the localized high heating regions on the windward surface. It is

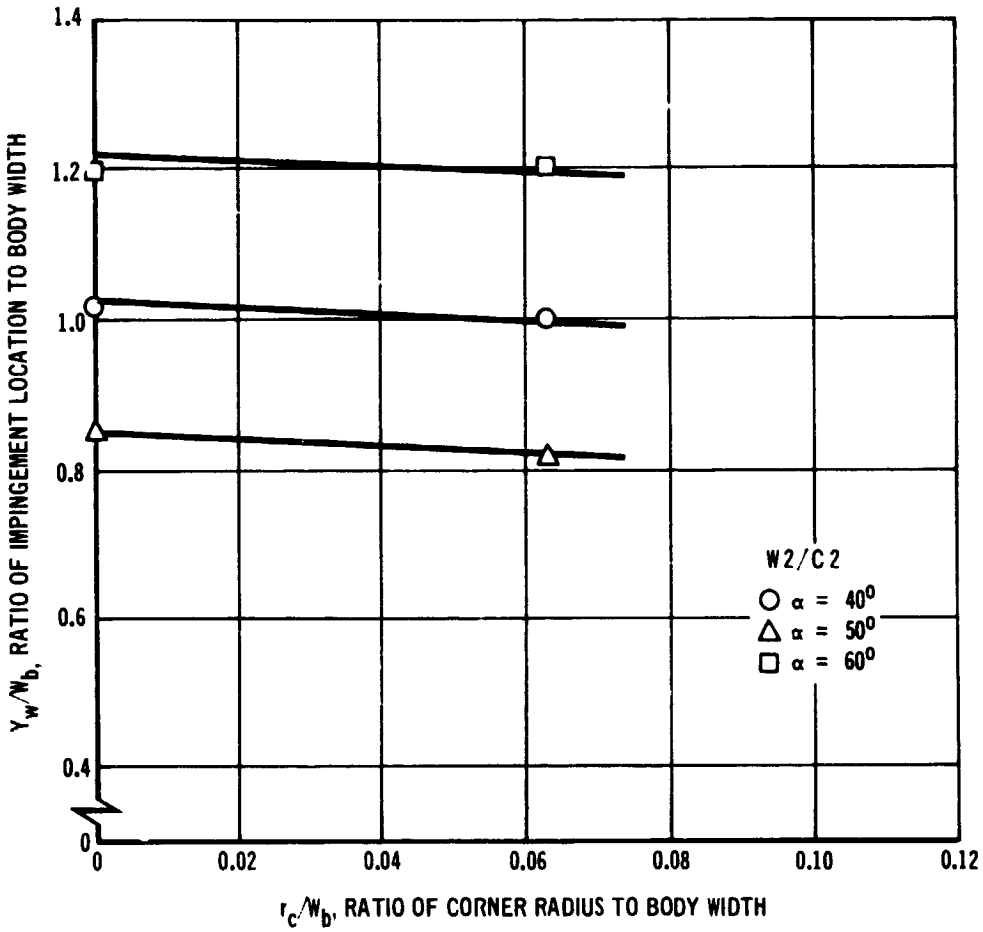

FIGURE 17 SHOCK INTERSECTION LOCATION AS A FUNCTION OF CORNER RADIUS

concluded that the observed shock impingement phenomena changes markedly at some critical angle of attack (clearly depending on configuration). This result agrees with the body-wing shock intersection data, which also indicate a significant change in the shock intersection location near 60 degree angle of attack.

Figure 18 shows the inboard and outboard impingement points defined by the high local heating on the wing leading edge. The effect of body corner radius is similar to that exhibited by the body-wing shock intersection data. As the corner radius increases, the impingement point moves inboard slightly for 30, 40, and 50 degree angles of attack. The 60 degree angle of attack burn data gave no indication of shock impingement on the wing. Therefore, at 60 degrees angle of attack, although the aerodynamic loads on the wing are higher than at the lower angles, the wing is not subjected to the localized high shear flow heating generated by the body-wing shock intersection.

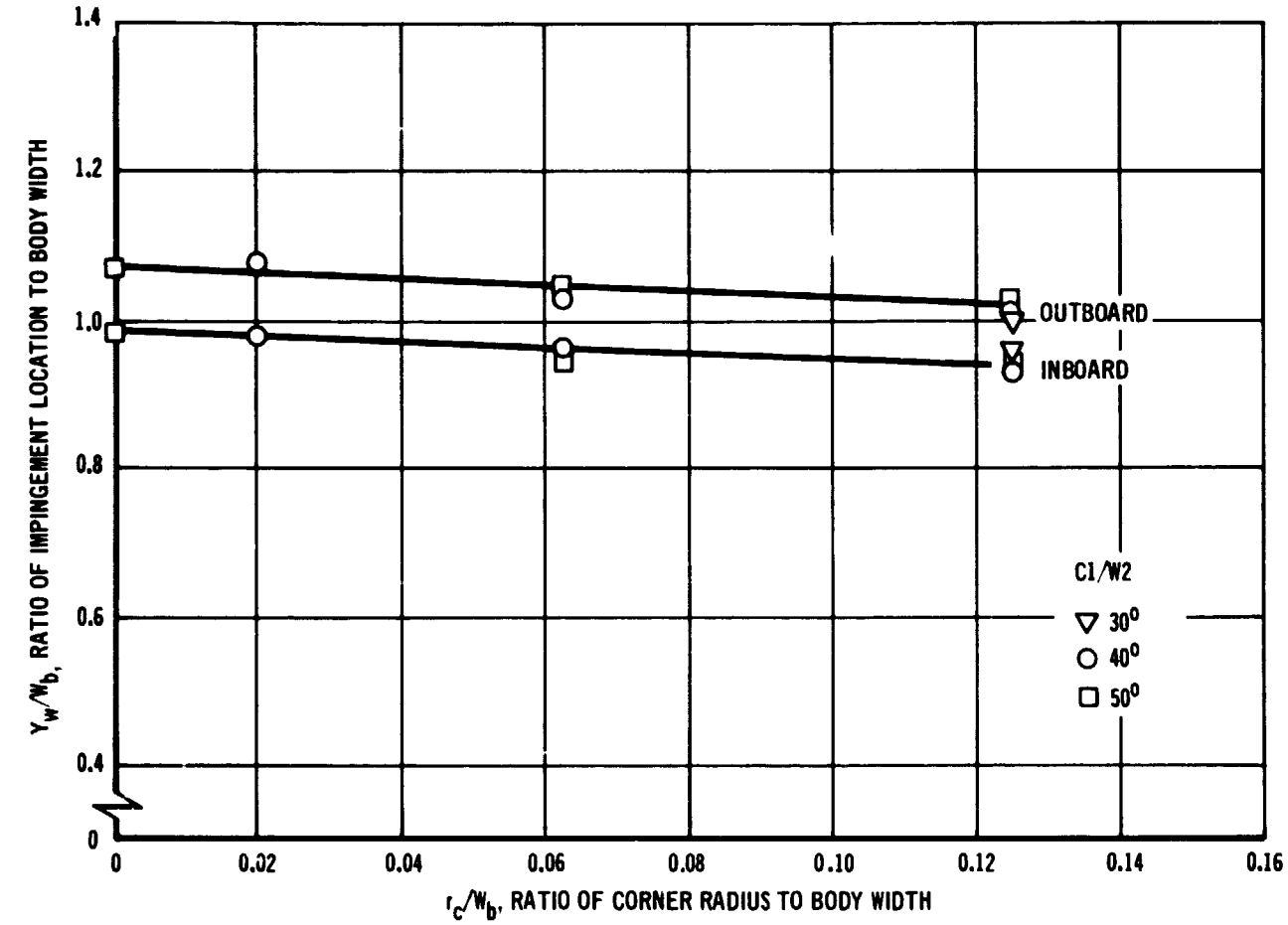

FIGURE 18 WING IMPINGEMENT LOCATION AS A FUNCTION OF CORNER RADIUS

Thermographic Mapping - The thermographic phosphor data indicate that, at 40 and 50 degree angles of attack, only one high local heating rate line is observed on the leeward surface of the wing. This heating line emanates from the leading edge shock impingement regions observed in the windward surface burn pattern (these trends are indicated by figure 19). The windward burn data were characterized by an "M" shaped pattern where vertices are at the leading edge associated with the wing-body shock interaction. Thus, a region of high heating is observed on both the windward and leeward surface. From the 40 and 50 degree angle-of-attack data, it can be postulated that the interior flow field which yields both an inboard and an outboard impingement pattern generated by the shock intersection, causes the outboard impingement to wrap around the wing to produce a high heating region on the leeward surface. Interior flow field properties must be such that the inboard shock strength is not sufficient to survive the rapid expansion to the leeward surface and, therefore, does not result in any local leeward heating problems.

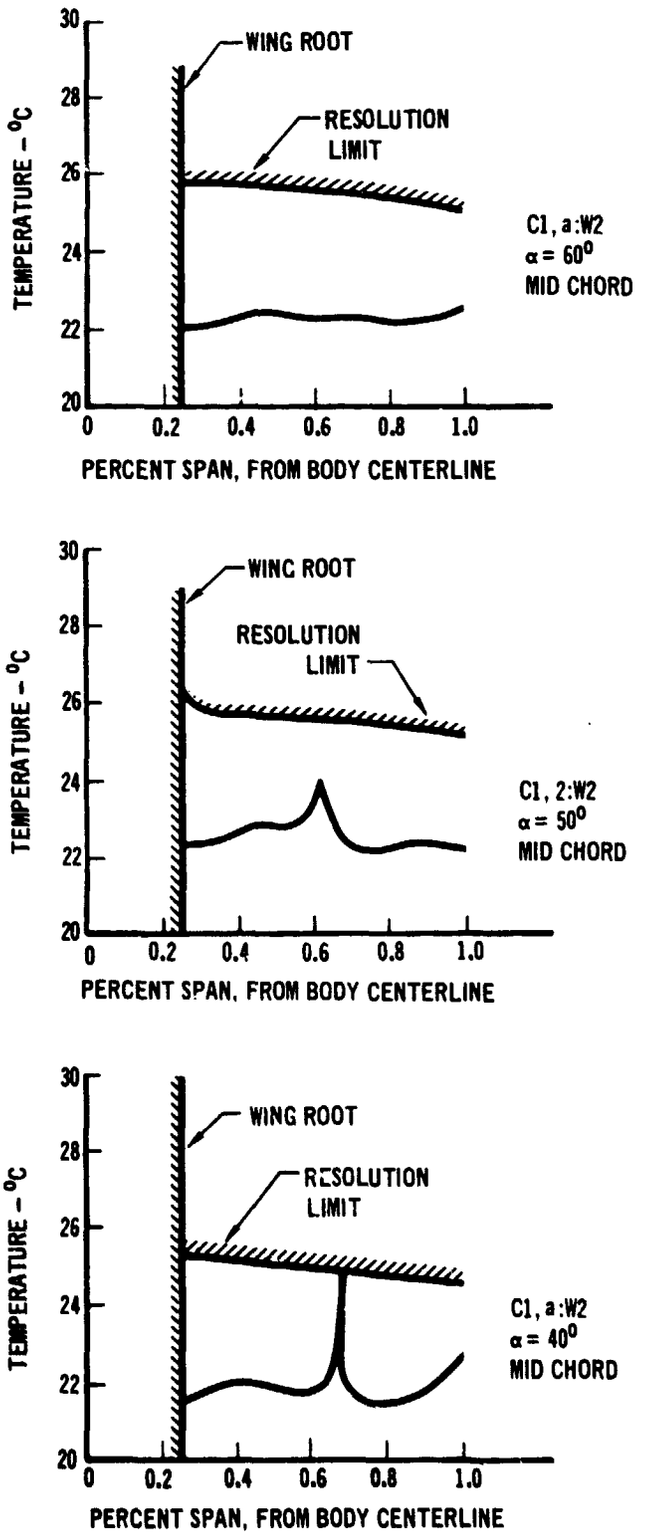

FIGURE 19 LOCAL TEMPERATURE AS A FUNCTION OF SPAN LOCATION

Flow Field - Relating the observed experimental data to an accurate flow model describing the body-wing shock intersection and resulting wing impingement phenomena is a difficult task. The data indicate that the shock intersection and wing impingement location move inboard with increasing angle of attack. At some critical angle of attack, signs of shock intersection, and resulting wing impingement, disappear. It is clear that a change in the interaction and impingement phenomena occurs, but it is not obvious what form the resulting flow structure takes.

In reviewing the wing-body shock intersection and wing impingement phenomena, an attempt has been made to relate the schlieren and burn data, obtained in the current program, to the shock interaction patterns classified by Edney[3] and the flow model proposed by Seegmiller[6]. Figure 20 presents Seegmiller's intersection and impingement model. The current results from burn data and limited thermal

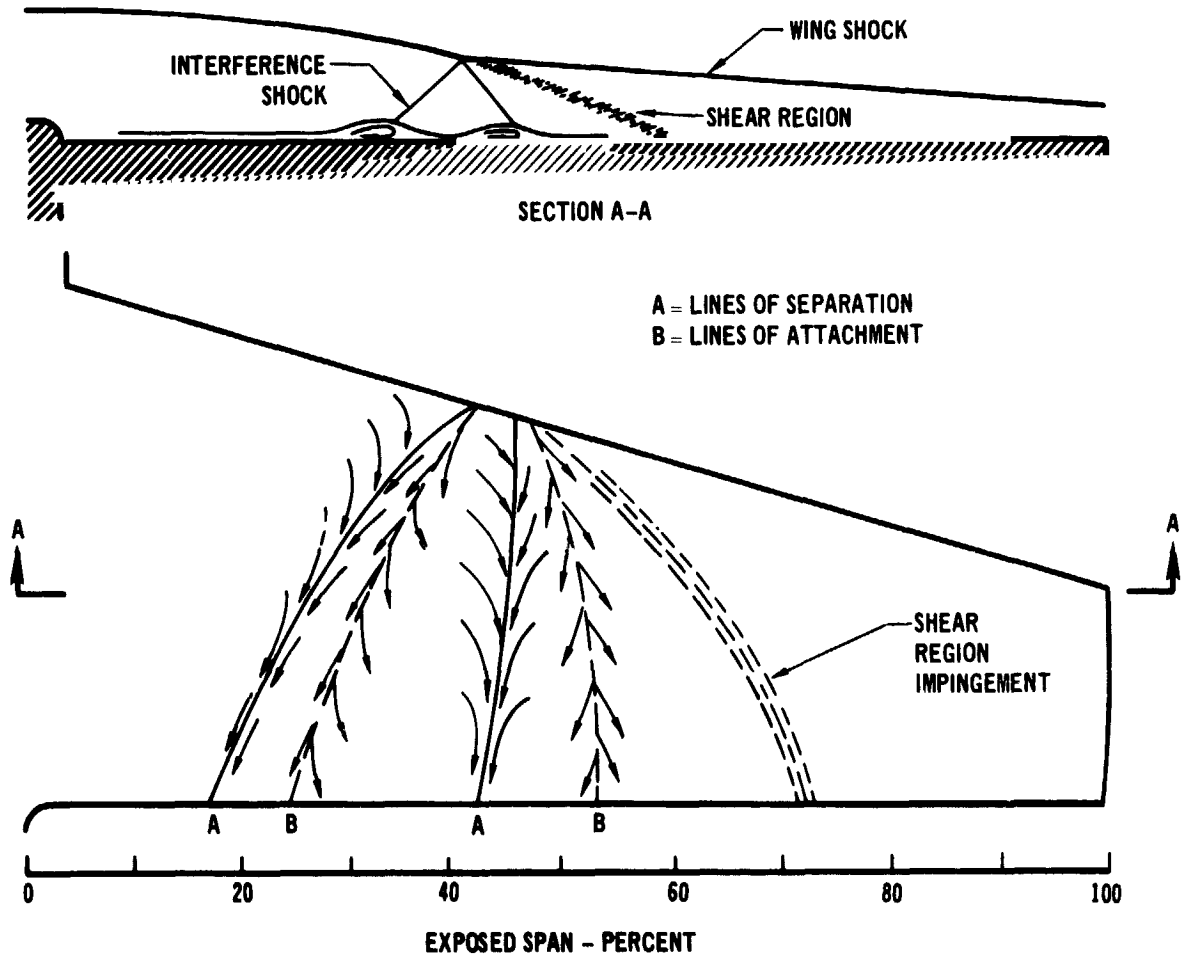

FIGURE 20 PROPOSED FLOW MODEL (REFERENCE 6)

phosphor data are in agreement with the flow pattern Seegmiller postulates on the windward surface (also substantiated with excellent quality oil flow data[6]). The shock intersection pattern, based on a cross-flow assumption proposed by Seegmiller does not agree with out current calculations. MDAC-EAST has investigated a cross-flow model (similar to Seegmiller's) as a degenerate case of the complex three-dimensional shock phenomena. Using the cross-flow analogy, the bow shock structure over the configuration cross-section was determined with the "time-dependent" technique developed by Moretti[7]. Likewise, the shock structure calculation was made for the wing assuming no influence from the body. Results of these calculations are shown in figure 21 for a freestream specific heat ratio (γ) of 1.2. The calculation of the shock/shock intersection pattern did not result in a converged slip line and, therefore, cannot be described by simple theories. No attempt was made here to construct the shock intersection pattern in the cross-flow plane due to the restrictive nature of the cross-flow assumption. Because of the relative strengths of the body and wing shocks, it is clear that a complex multishock pattern would develop, along with regions of high shear. The formation

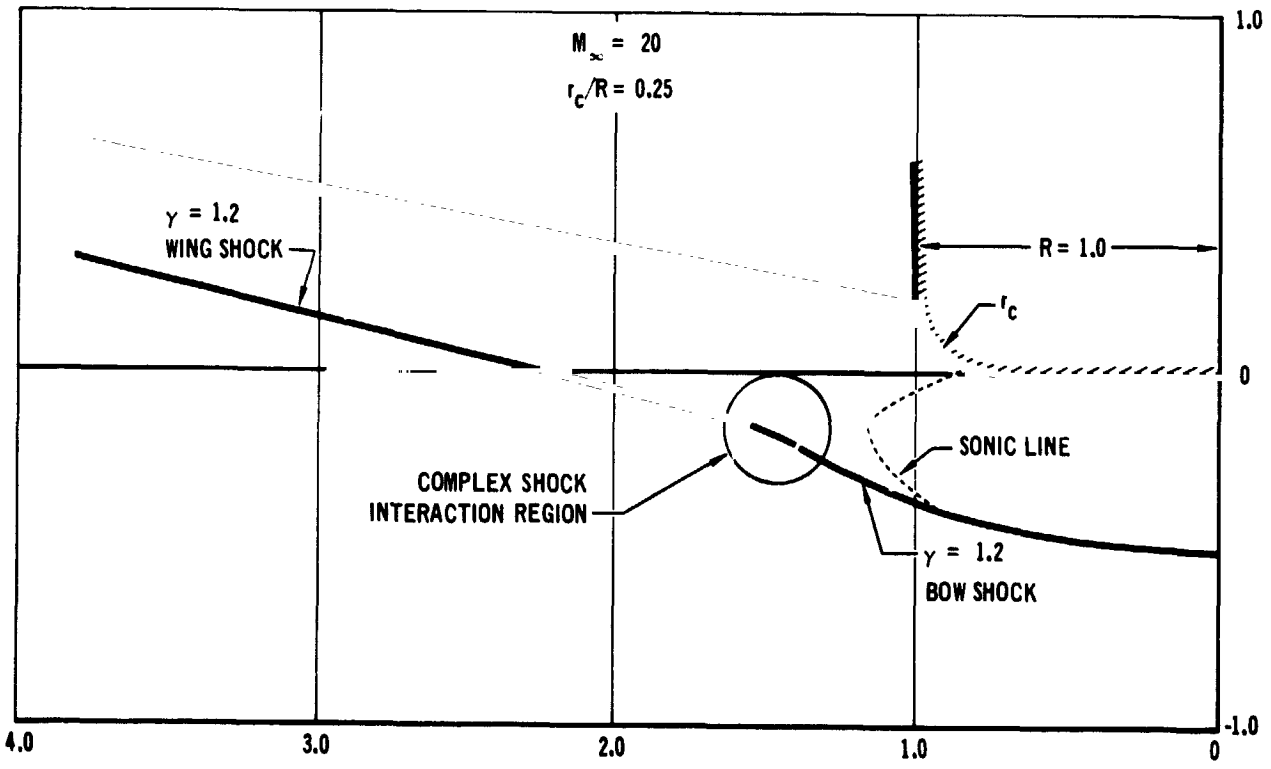

FIGURE 21 CROSS-FLOW ANALYSIS

of a transmitted and reflected shock in Seegmiller's model requires that the flow behind the bow and wing shocks are supersonic in the cross-flow plane. In the MDAC-EAST cross-flow calculations, a supersonic Mach number was obtained behind the wing shock only by allowing the wing to have dihedral. It is, therefore, questionable that a 40 degree angle-of-attack flow pattern can realistically be modeled by a cross-flow analysis.

The three-dimensionality of the flight vehicle flow field makes it virtually impossible to discuss systematically the intersection and resulting wing impingement phenomena. Not only do the basic shock envelopes (body and wing) depend strongly on the configuration and freestream conditions, but the relative angles and strengths of these shocks change markedly with angle of attack and peripheral location. Thus, it is clear that one shock intersection pattern does not completely define the intersection phenomena, even at a single angle of attack.

The 60 degree experimental data (burn photographs) did not indicate any signs of windward surface shock impingement, while lower angle-of-attack data (40 and 50 degree) show a distinct impingement pattern on the windward surface. The lower angle-of-attack windward surface impingement pattern was investigated considering the transverse Mach number component in the body planform plane. Instead of postulating a new interaction pattern, the interaction classification types proposed by Edney[3] were considered. Figure 22 shows a "type V" shock-shock interaction over a typical straight wing. The flow model agrees with the current test schlieren photographs, since a thickening of the shock layer over the wing is predicted (observed in the 40 and 50 degree, planform view, schlieren photographs). Although the reflected shock, supersonic jet, and shear layer may describe the observed impingement results on the windward surface, a complete flow model definition is outside the scope of this study and beyond the current state of the art. However, Edney's type V interaction model does fit the current test data and Seegmiller's oil flow data.

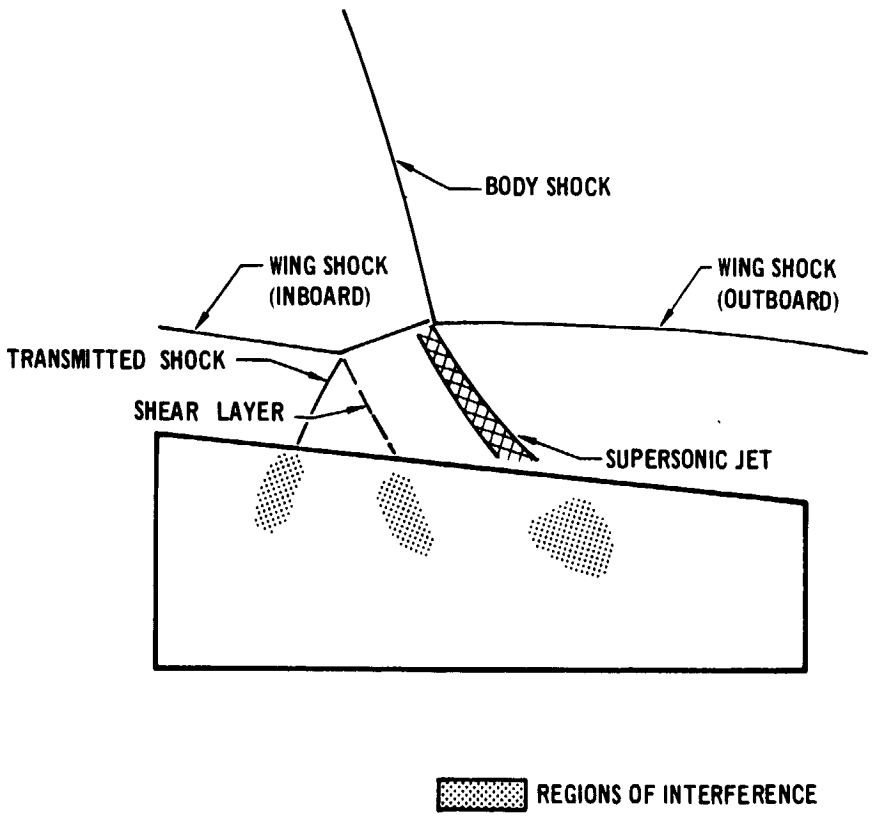

FIGURE 22 SCHEMATIC OF EDNEY'S TYPE V INTERACTION WITH RESULTING IMPINGEMENT REGIONS

6. CONCLUSIONS

Results of wind tunnel investigations on Space Shuttle body-wing configuration show that both the body shock-wing shock intersection point and the wing leading edge impingement point move inboard as angle of attack increases up to some critical angle of attack. At this critical angle of attack, the body and wing shocks merge into one equivalent cruciform blunt body shock. The shock intersection point and the wing body edge impingement point then move rapidly outboard. Due to the limited data (60 degree angle of attack only) above this "critical" angle of attack the exact functional dependence on angle of attack of the movement of these parts cannot be defined.

Similarly, wing leading edge impingement heating does not occur at 60 degree angle of attack. The wing impingement heating pattern for the 40 and 50 degree angle of attack test results is characterized by an "M" shaped heating pattern on the windward surface with the vertices of the "M" at the leading edge. The only strong leeward surface heating pattern is one interference streak emanating from the leading edge outboard vertex of the "M." The inboard vertex does not generate a strong leeward surface heating pattern since it is postulated as the impingement of a reflected shock whose strength is too low to survive the expansion around the wing leading edge.

The leeward surface heating data indicate that the inboard impingement trace is much weaker than the outboard pattern. This trend is consistent with the postulation that the rapid expansion significantly weakens the reflected shock wave.

It is presently impossible to specify and calculate the flow field properties resulting from shock/shock intersection phenomena on Space Shuttle vehicles. However, the "type V" shock interaction class of Edney[3] best explains the results obtained in this program.

The data obtained in this program provide insight into the highly complex shock wave intersection and impingement phenomena associated with Space Shuttle vehicles.

7. REFERENCES

1. Lays, E. J. and Gearhart, L. M. "Hypervelocity and Driven Impulse Tunnel Description and User Information," Martin-Marietta Report No. M-68-17, September 1968.

2. Grabau, Humphrey, and Little, "A Data Reduction Program for Hotshot Tunnels Based on the Faye-Riddell Heat-Transfer Rate Using Nitrogen at Stagnation Temperatures from 1500 to 5000°K," AEDC-TDR-64-50.

3. Edney, B. E., "Shock Interference Heating and the Space Shuttle," NASA TMX-52876, July 1970.

4. Seiff, A. and Whiting, E. E., "Calculation of Flow Fields from Bow-Wave Profiles for the Downstream Region of Blunt-Nosed Circular Cylinders in Axial Hypersonic Flight," NASA TND-1147, November 1961.

5. Mockapetris, L. R., Reilly, J. F., and Kessler, W. C., "Investigation of Cylinder Cross-Section Effect on Shock Structure and Surface Heating," to be published.

6. Seegmiller, H. L., "Shock Interference Heating and Density-Ratio Effects: Part I - Flow Field Visualization, Thermocouple Measurements and Analysis," NASA TMX-2272, March 1971.

7. Moretti, G. and Abbett, M., "A Time-Dependent Computational Method for Blunt Body Flows," AIAA Journal, Vol. 4, No. 12, December 1966.